RSC Advances

PAPER

View Article Online
View Journal | View Issue

Cite this: *RSC Adv.*, 2021, **11**, 22079

Porous hydrogen substituted graphyne as a promising anode for lithium-ion batteries†

Bo Wan,[a] Qian He,[b] X. G. Wan[a] and Qingfang Li*[b]

Received 30th April 2021
Accepted 7th June 2021

DOI: 10.1039/d1ra03396d

rsc.li/rsc-advances

Porous hydrogen substituted graphyne (HsGY) has been considered as a promising candidate for anode material due to its excellent electrochemical properties. In this work, we found that monolayer and bilayer HsGY are good electrodes for high charge capacity lithium-ion batteries based on density functional theory calculations. Mechanical tests reveal that monolayer and bilayer HsGY exhibit excellent mechanical properties, including large critical strains (>25%) and high in-plane stiffness (>200 N m^{-1}). The bilayer HsGY displays ultrahigh stiffness (400.27 N m^{-1}). Li adsorption on bilayer HsGY is stronger than that on the monolayer HsGY. Moreover, Li diffusion on the surfaces of monolayer and bilayer HsGY has low energy barriers (<0.5 eV). Our calculation results suggest that HsGY may contain the highest theoretical charge capacity among two-dimensional (2D) materials studied so far, with ultrahigh Li capacities of 3378 and 2895 mA h g^{-1} for monolayer and bilayer HsGY, respectively. Given these advantages, including large critical strain, high mechanical stiffness, strong adsorption, low diffusive energy barrier, and high charge capacity, we conclude that both monolayer and bilayer HsGY could be promising anode materials for lithium-ion batteries.

1. Introduction

With recent rapid development of portable electronics, mobile communication devices and electric vehicles, Li-ion batteries (LIBs) have attracted great attention due to their high safety, light weight and long lifespan.[1,2] Among various LIBs, ultrathin LIBs hold great promise in portable electronic equipment, such as integrated circuit smart cards, wearable health devices, roll-up displays and flexible solar panels.[3–7] Typically, LIBs consist of two electrodes: the anode and cathode. Because the properties of the anode materials determine the crucial lithium-ion batteries (LIBs) characteristics, such as cycling life, capacity and charge/discharge rate, suitable anode materials are critical for LIBs.[8] The conventional anode materials, typically made of materials such as graphite and oxides, can easily crack or delaminate under mechanical strain.[9,10] In this regard, it is essential to develop high-performance anode materials of LIBs with large critical strains.

Two-dimensional (2D) materials have been widely investigated as anode materials for rechargeable LIBs owing to their extraordinary electrochemical properties, and unique morphology which offers more insertion channels and enables fast metal-ion diffusion.[11–14] Because of their abundance, affordability and chemical stability, the carbon-based 2D materials are most widely used in metal-ion batteries. As a representative member of carbon-based 2D materials, graphene shows good electrochemical performance and long cyclability.[15] However, the limited storage capacity (540 mA h g^{-1})[15] impedes its practical application in LIBs. The discovery of graphynes (GYs)[16] with uniform nanopores and low atomic density provides a new choice for the lithium storage. GYs are composed of sp and sp^2 hybridized C atoms. The members of GYs family include α-GY, β-GY, γ-GY, graphdiyne (GDY) and β-GDY *etc.*[16–18] Compared with the graphene composed merely carbon hexagons, the asymmetrically conjugated π electrons and located large pores endow the GYs with a more promising prospect in LIBs.[19–24]

Recently, a new member of the GYs family, the porous hydrogen substituted GY (HsGY) nanosheets was synthesized using the facile bottom-up synthetic approach.[25] The experiments showed that the flexible HsGY films as the anode in lithium and sodium ion batteries exhibited excellent electrochemical properties.[25,26] A high initial Li charge capacity of 1640 mA h g^{-1} under 50 mA g^{-1} was found in the HsGY-based electrode, and the reversible capacity of ~1550 mA h g^{-1} can be stabilized.[26] It was reported that the reversible Na storage capacity reached as high as 580 mA h g^{-1} after 200 charge/discharge cycles,[25] and the theoretical simulations demonstrated the HsGY monolayer could provide numerous Na storage sites and delivered Na storage capacity of 1207 mA h g^{-1}.[25] Li *et al.*[27] also synthesized HsGY film by alkyne metathesis reaction and demonstrated that HsGY can be used

[a]*National Laboratory of Solid State Microstructures and School of Physics, Nanjing University, Nanjing 210093, China*

[b]*School of Physics & Optoelectronic Engineering, Nanjing University of Information Science & Technology, Nanjing 210044, China. E-mail: qingfangli@nuist.edu.cn*

† Electronic supplementary information (ESI) available. See DOI: 10.1039/d1ra03396d

as lithium–sulfur battery. As anode material of LIBs, HsGY was revealed to have high capacity and excellent cycling stability.[26] However, the intrinsic mechanisms of charge and discharge of HsGY as LIBs are still unclear. Motivated by the successful synthesis of HsGY involving excellent electrochemical performance, we performed first-principles simulations to probe the feasibility of monolayer and bilayer HsGY as anode materials for LIBs.

2. Computational details

All the first-principles calculations in this paper were performed using the Vienna *ab initio* simulation package (VASP).[28,29] The projector-augmented plane wave potential[30] was used to calculate the electron–ion interactions, and the electron exchange–correlation interactions were described using the generalized gradient approximation in the form of Perdew, Burke, and Ernzerhof (PBE) functional.[31] The van der Waals (vdW) interactions (DFT-D2 method of Grimme)[32] was employed for all simulations. The kinetic energy cutoff of 520 eV was adopted. A k-mesh of $5 \times 5 \times 1$ was used for the structural optimization. The lattice vectors and atomic coordinates were fully relaxed until the energy and force convergence thresholds reach 0.01 eV $Å^{-1}$ and 10^{-6} eV, respectively. The primitive cell is adopted to model all adsorption systems. The $2 \times 2 \times 1$ supercell was also used to test the Li adsorption behavior. It is found that the adsorption energy per lithium atom hardly change with the increasing of supercell size. The vacuum regions of 20 Å and 25 Å were placed in the z direction for monolayer and bilayer HsGY, respectively. The climbing image nudged elastic band method[33] was applied to obtain the Li-ions migration paths and diffusion energy barriers. The average adsorption energy resulting from the interactions between monolayer (bilayer) HsGY with Li atoms is defined as:

$$E_{ad} = \frac{E_{HsGY+nLi} - nE_{Li} - E_{HsGY}}{n} \quad (1)$$

where $E_{HsGY+nLi}$ and E_{HsGY} represent the total energies of monolayer (bilayer) HsGY with and without Li adatoms, respectively. E_{Li} and n denote the total energy of an isolated Li atom and the number of lithium atoms, respectively.

3. Results and discussions

We first optimize the geometric structures of monolayer and bilayer HsGY. As displayed in Fig. 1a, the HsGY monolayer has a hydrocarbon skeleton with space group *P6/mmm*. The primitive cell is a planar hexagonal cell with the optimized lattice constant of 11.926 Å. There are C_1 (sp), C_2 ($2p^2$) and C_3 ($2p^2$) three different C atoms which form C_1–C_1, C_1–C_2 and C_2–C_3 three different kinds of C–C bonds. For bilayer HsGY, we consider four possible stacking structures, namely AA-, AB-, AC- and AD-stacking, as indicated in Fig. 1. In Fig. 1b, the top layer of AA-stacking can be viewed as vertically stacking on the bottom layer. AB-stacking (Fig. 1c): the upper layer of AA-stacking is shifted by one-third of one unit cell along the x direction of the hexagonal cell. AC-stacking (Fig. 1d) and AD-

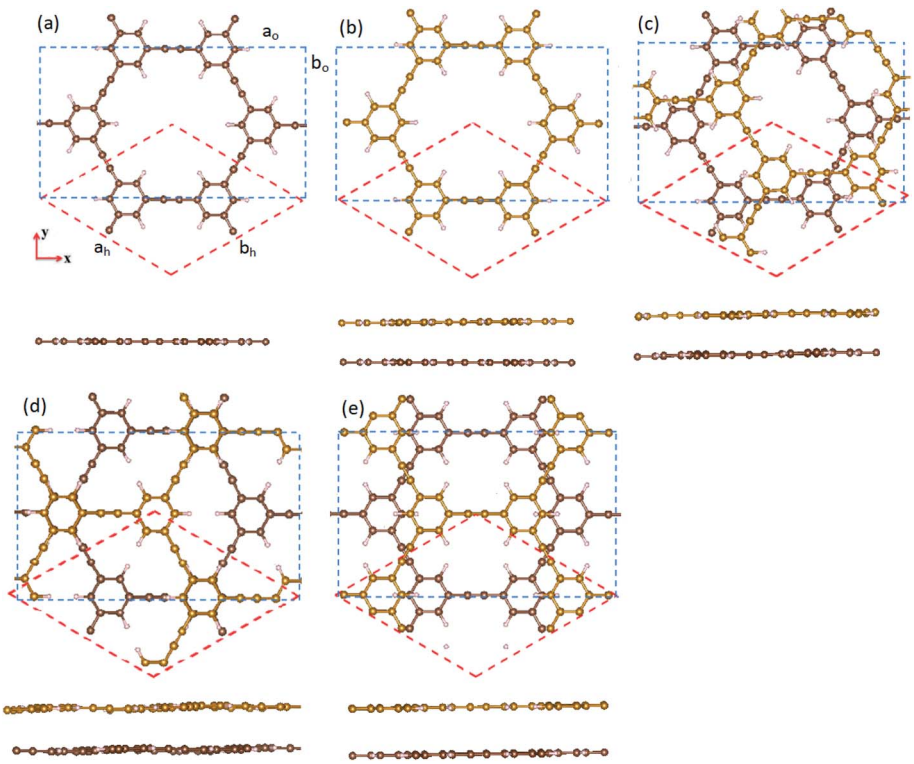

Fig. 1 (a) Top and side views of monolayer HsGY.(b–e) AA, AB, AC and AD stacking structures, respectively. The orthogonal supercell is indicated by the blue dashed lines. The yellow and brown balls are the C atoms on upper and bottom layers, respectively. The white balls are the H atoms.

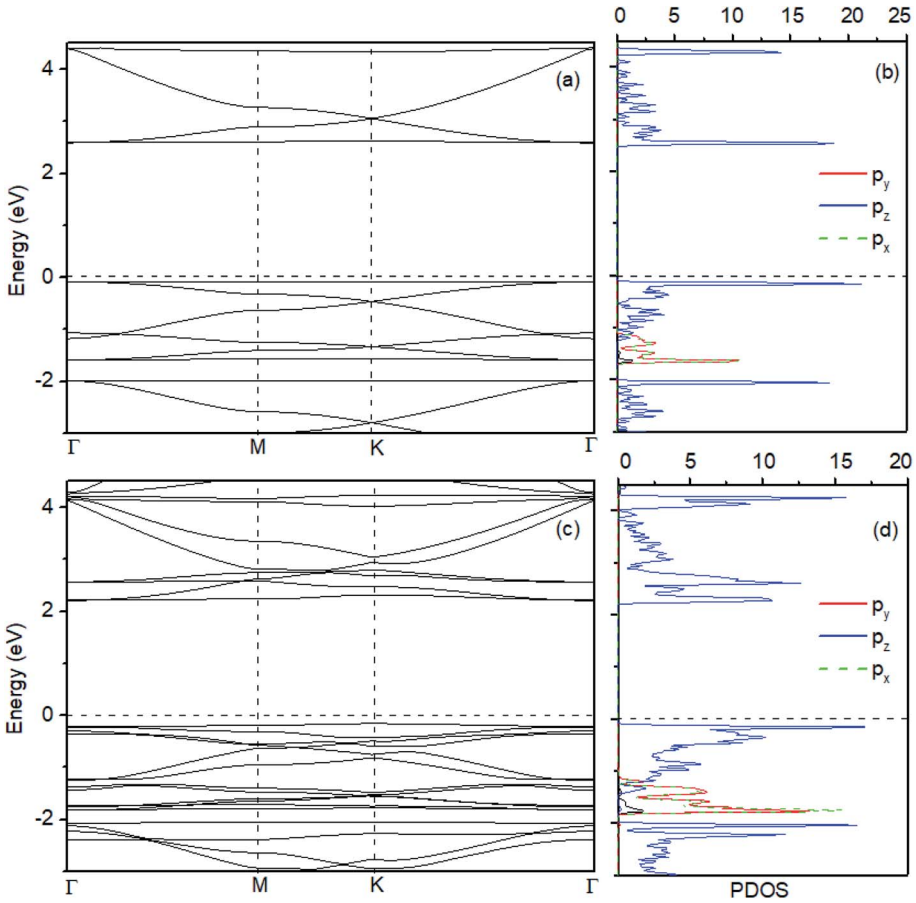

Fig. 2 (a) Band structure, and (b) PDOS of monolayer HsGY. (c) Band structure, and (d) PDOS of bilayer HsGY.

stacking (Fig. 1e) can be looked as the shift of the top layer of AA-stacking along the x or y axis for half of the orthogonal supercell. To confirm the stability of bilayer HsGY, the formation energy is calculated as $E_f = (E_b - E_{up} - E_{low})/n$, where E_b, E_{up} and E_{low} represent the total energies of HsGY bilayer, upper layer HsGY and lower layer HsGY, respectively. n denotes the number of atoms in the bilayer HsGY. The formation energies are −190.65, −240.87, −227.70 and −195.17 meV per layer. The AB-stacking bilayer HsGY is the most favorable configuration, and the corresponding lattice constants are $a = b = 11.915$ Å. Therefore, we only discuss the results of the AB-stacked bilayer HsGY in the following.

Then, we investigate the electronic properties of monolayer and bilayer HsGY. The characters of the band structures based on the HSE06 method is similar with those based on PBE method.[34] Therefore, we only discuss the corresponding results based on PBE method. As indicated in Fig. 2, the band structures demonstrate that both monolayer and bilayer HsGY are semiconductors with band gaps of 2.67 and 2.36 eV, respectively. One can notice that there are a flat energy band and two Dirac energy bands at either side of the Fermi level in monolayer HsGY, while the Dirac bands are broken in bilayer HsGY which is attributed to the vdW interaction between two layers. To further clear the electronic properties, their partial density of states (PDOS) are also shown in Fig. 2. For both monolayer and bilayer HsGY, the states of the valence band maximum and the conduction band minimum originate from the p_z orbitals of C atoms.

To explore the mechanical properties of monolayer and bilayer HsGY, tensile calculations in an orthogonal supercell are performed (Fig. 1a and c). The uniaxial stress–strain relations of monolayer and bilayer HsGY along x (armchair) and y (zigzag) directions are displayed in Fig. 3. For monolayer HsGY, the tensile strengths along x and y are 28.66 GPa and 29.32 GPa, corresponding to the failure strains of 26% and 27%, respectively. The peak stresses for the bilayer HsGY are 34.66 GPa and 35.53 GPa in the x and y directions, and their critical strains are 25% and 26%, respectively. Note that, the stress–strain responses for both monolayer and bilayer HsGY abruptly change when the strains reach their critical values, implying that the atomic structures of monolayer and bilayer HsGY have a significant transformation. Furthermore, the in-plane stiffness is fitted by the equation:

$$C = \frac{1}{S_0}\frac{\partial^2 E}{\partial \varepsilon^2} \quad (2)$$

where S_0 and E are the area of equilibrium structure and the total energy. ε is the strain applied on the HsGY. When the applied strain is in the range of −1% to 1%, the calculated in-plane stiffness of monolayer HsGY is 200.48 N m^{-1}, which is

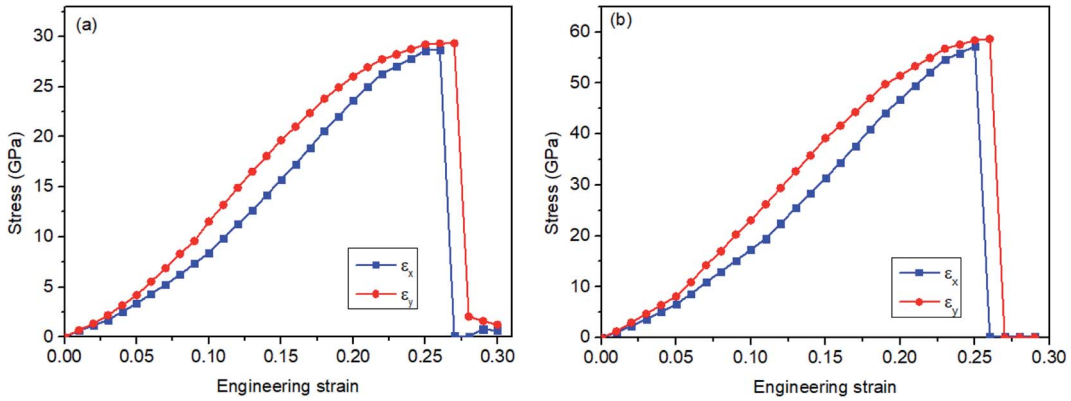

Fig. 3 Stress–strain relationships under uniaxial *x* and *y* directions of (a) monolayer HsGY and (b) bilayer HsGY.

larger than that of C_{68}–GY (50.5 N m^{-1})[35] but smaller than that of graphene (350 N m^{-1}).[36] Interestingly, the bilayer HsGY displays ultrahigh stiffness (400.27 N m^{-1}), which is about 2 times as large as that of monolayer HsGY. The high stiffness of bilayer HsGY is vital as its application in LIBs, due to the large deformations and stresses caused by the lithium insertion/extraction.

As a anode material for LIBs, it is essential to understand the adsorption behavior of Li on HsGY. To examine the adsorption ability of HsGY, all possible adsorption sites are considered. For one Li adsorption on monolayer HsGY, the stable adsorption sites are displayed in Fig. 4a: (1) H_1 site: hollow site on the center of hexagon carbon ring; (2) H_2 site: hollow site between H and C atoms; (3) B site: bridge site between C and C atoms. The lowest adsorption energy (−1.91 eV) corresponds to the H_1 adsorption site. The nearest-neighbor Li–C bond length is 2.24 Å. The adsorption energies of H_2 and B sites are 0.20 and 0.31 eV higher than that of the most stable configuration. The H_1 adsorption sites remain the most stable sites for two and four Li atoms adsorption. The corresponding adsorption energies are −1.77 and −1.63 eV per atom, respectively. For six-atom adsorption case, two Li atoms reside on the H_2 sites, and slight wrinkle is observed in the C_1–C_1 bond which is formed by sp–sp hybridization. Further increasing Li atoms will enhance the structural deformation of HsGY as shown in Fig. 3. The monolayer HsGY can adsorb up to 28 Li atoms, and the system can return back to its original structure by removal of Li atoms.

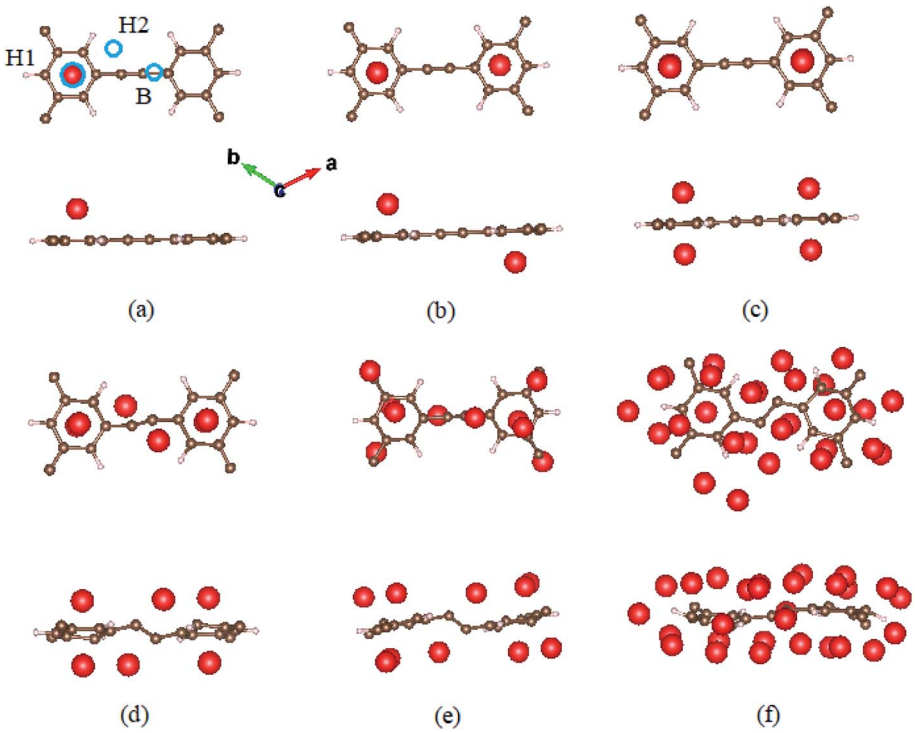

Fig. 4 Optimized structures of lithiated monolayer HsGY. (a) One Li, (b) two Li, (c) four Li, (d) six Li, (e) ten Li, and (f) twenty-eight Li atoms adsorbed on HsGY.

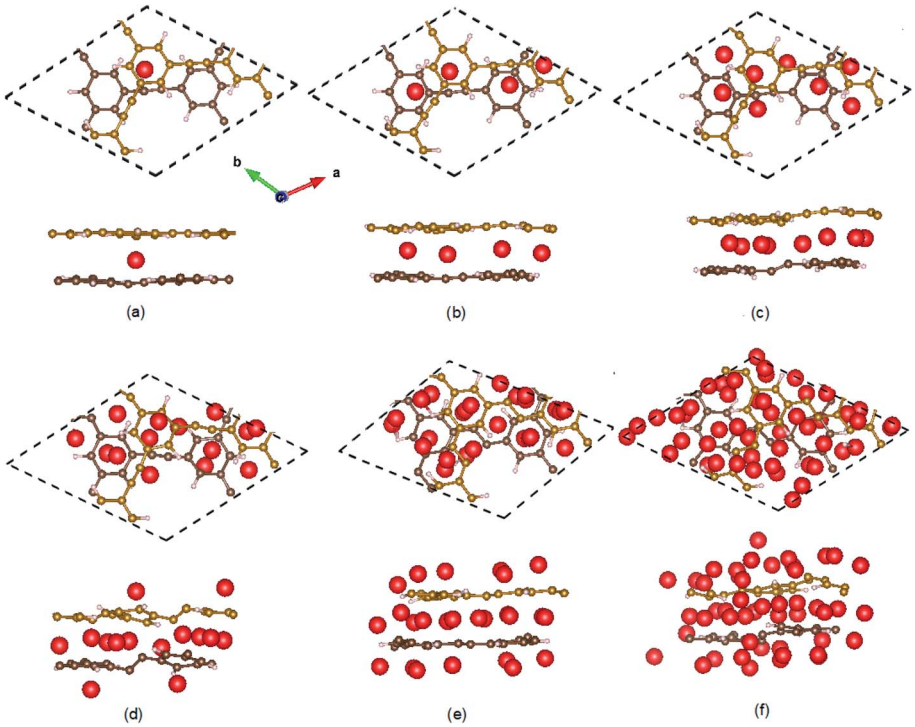

Fig. 5 Optimized structures of lithiated bilayer HsGY. (a) One Li, (b) four Li, (c) eight Li, (d) fourteen Li, (e) twenty-six Li, and (f) forty-eight Li atoms adsorbed on HsGY.

Now we turn to the structures of lithiated bilayer HsGY (Fig. 5). For one adatom in bilayer HsGY, Li atom adsorbs preferably at the hollow site between two layers with $E_{ad} = -2.42$ eV. The adsorption configuration with one Li atom on the H_1 site of the external layer is less favorable, and the adsorption energy is -1.41 eV. For four-atom and eight-atom adsorption configuration, the intermediate layer is still preferentially occupied by Li atoms as displayed in Fig. 5b and c. The Li atoms gradually occupy external surfaces with increasing lithium concentration. For 48 Li atoms, a third of lithium atoms reside in the interior area, and the other adatoms occupy the hole sites and bridge sites of external surfaces. An ideal anode material for LIBs must meet the requirement: The average adsorption energy of per Li is larger than the experimental binding energy of Li (1.63 eV) in the bulk lattice and smaller than 3.0 eV.[37,38] The case of bilayer layer adsorption can well meet this requirement.

The calculated results indicate that the adsorption energy of Li in bilayer HsGY is higher than that in monolayer HsGY for all considering Li coverage, which means that the Li adatoms bind stronger with the bilayer HsGY, and the lithiated bilayer HsGY is more stable than the monolayer one. Going from the pristine HsGY to the lithiated monolayer (bilayer) HsGY with the highest Li content, the energy difference spans only 0.32 (0.49) eV. Therefore, the working potential of an electrode based on monolayer and bilayer HsGY should be relatively flat, which happens to be one attractive feature of anode materials for lithium-ion batteries. To understand the trend of adsorption energies, we calculate the charge transfers between adatom and HsGY. The calculated results indicate that each Li adatom donates about $0.88 \sim 0.92e$ to C, which results in partially cationic lithium. The ionic components mostly dominate the chemical bonds between Li and C. On the other hand, the repulsion among lithium ions and surface reconstruction become larger with increase of adatom concentration. The cooperative effects of the static charge transfer, the repulsive interaction and surface reconstruction result in the subtle changes of adsorption energies in monolayer and bilayer HsGY. At low Li concentration, the adsorption energies of monolayer and bilayer HsGY increase as the lithium concentration increases, which mainly attributes to the increasing repulsive interaction. The adsorption energy change characteristics of Li on the HsGY are similar to those of monolayer/bilayer blue phosphorus.[39] To realized the practical applications, the thermal stability of monolayer HsGY with 28 Li adsorption and bilayer HsGY with 48 Li adsorption is examined by *ab initio* molecular dynamics in the *NVT* ensemble. The supercells of monolayer and bilayer monolayer contain 208 and 192 atoms, respectively. Fig. S1† presents the calculated snapshots of top and side views. After heating at 300 K for 5 ps with the time-step of 1 fs, all Li atoms are well stabilized on HsGY, and both monolayer and bilayer HsGY are intact although they have a small corrugation.

The ionic intercalation potential is vital parameter that decisively affects the performance of the LIBs. Here, we calculate the insertion potential using the following open circuit voltage (OCV) equation:[40]

$$\mathrm{OCV} = -\frac{E_{C_{18}H_6Li_{x_2}} - E_{C_{18}H_6Li_{x_1}}\ (x_2 - x_1\ )E_{Li}}{(x_2 - x_1\ )} \qquad (3)$$

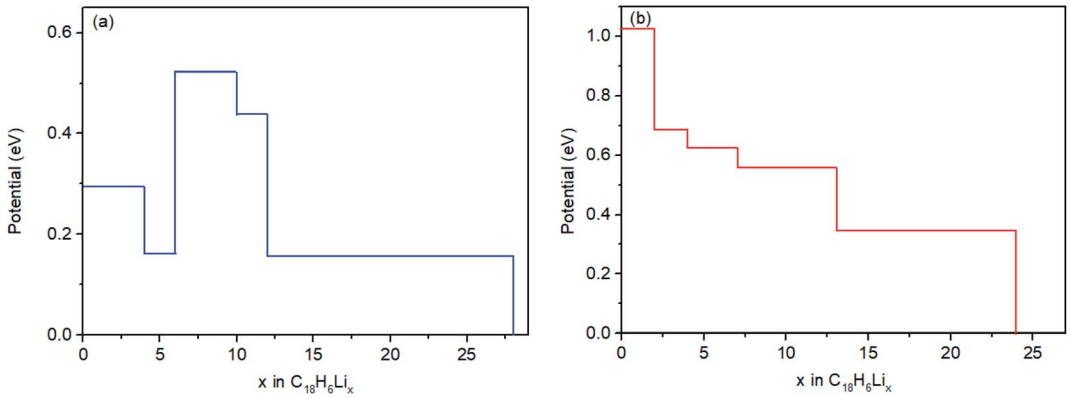

Fig. 6 The open-circuit voltage as the function of Li concentration of (a) monolayer HsGY and (b) bilayer HsGY.

where $E_{C_{18}H_6Li_x}$ is the total energy of the monolayer and bilayer HsGY adsorbing Li atoms, x_2 and x_1 represent the concentrations of Li ions on the HsGY surfaces, and E_{Li} is the energy per Li in the bulk lattice. As plotted in Fig. 6, it is found that the voltages of monolayer and bilayer HsGY are 0.16 ∽ 0.52 eV and 0.35 ∽ 1.03 eV, respectively. All values almost lie within the desired potential values of the promising anode materials.

The charge capacities are obtained with the following formula, $C_{th}=(F \times n_{Li})/(3.6m_{HsGY})$, where F is the Faraday's constant (96 500 C mol^{-1}), n_{Li} stands for the number of Li per formula unit of monolayer/bilayer HsGY ($C_{18}H_6Li_x$), and m_{HsGY} is the mass of monolayer/bilayer HsGY in $C_{18}H_6Li_x$. The calculated charge capacities of monolayer and bilayer HsGY are 3378 and 2895 mA h g^{-1}, respectively. The charge capacities of monolayer/bilayer HsGY are significantly higher than those of other 2D materials such as monolayer carbon ene–yne (CEY) (2680 mA h g^{-1}),[41] monolayer (1954 mA h g^{-1}) and bilayer (1675 mA h g^{-1}) C_{68}–graphyne.[35] To date, the CEY has been theoretically predicted to yield the highest charge capacities among all other 2D materials.[41] As it is clear, HsGY distinctly outperform not only the CEY but also the other 2D anode materials with respect to the storage capacities.

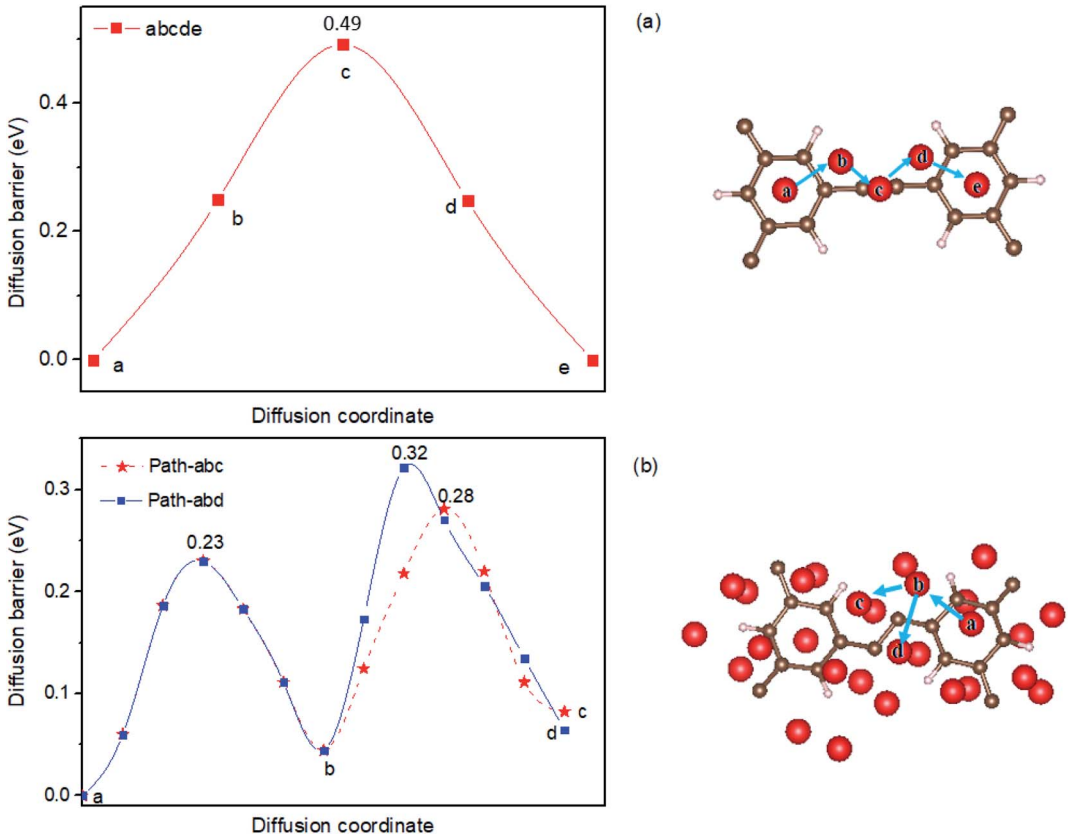

Fig. 7 Schematic representations and potential-energy curves of Li diffusion on monolayer HsGY.

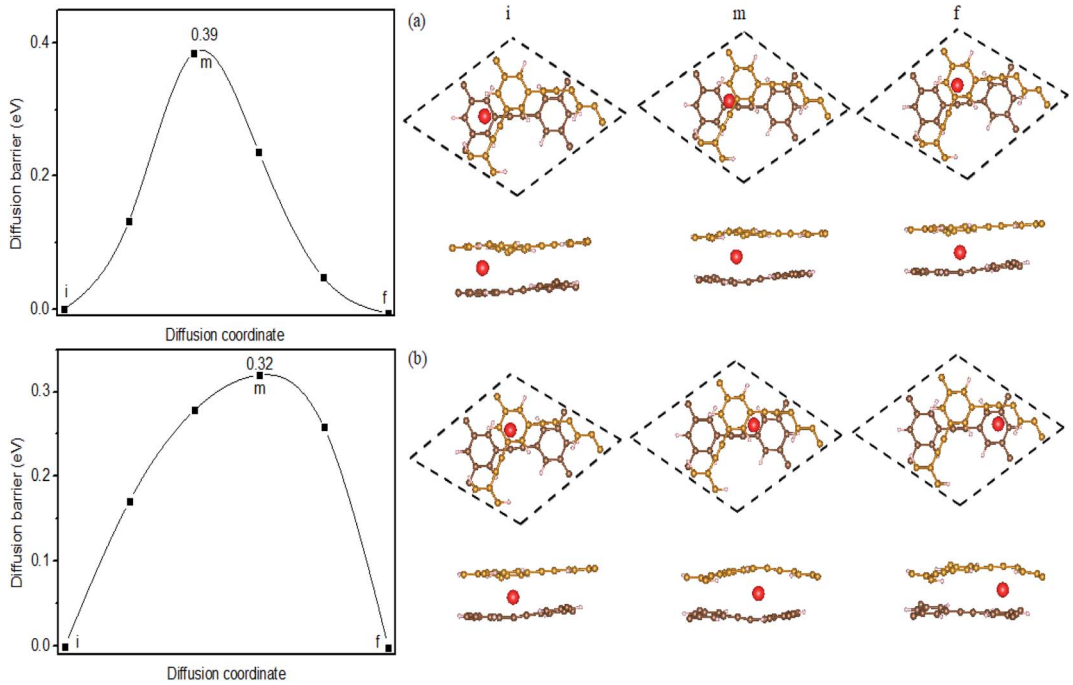

Fig. 8 Schematic representations and potential-energy curves of Li diffusion on bilayer HsGY.

It is well-known that the Li diffusion character is one important index of the rate performance in the electrode materials. Thus, we check the diffusion of Li adatom on monolayer and bilayer HsGY. For monolayer HsGY, H_1 site is the most stable adsorption site. Li atom occupies the H_1 site with the six nearest neighbor C atoms. As one Li at H_1 site moves towards the nearest neighbor H1 site, Li passes over the C–C bridge site along the armchair direction by overcoming a barrier of 0.49 eV (Fig. 7a). In the high coverage, one Li diffusion is modeled by removing one Li from the highest lithium coverage as shown in Fig. 7b. The H_2 site is the second stable adsorption site. As one Li atom hops from H_1 to its nearest neighbor H_2, it overcomes an energy barrier of 0.23 eV. And the diffusion energy barriers are 0.28 and 0.32 eV, if the Li atom at H_2 continues to move to its adjacent H2 along and across the –C≡C– link, respectively. For bilayer HsGY, one Li prefers to occupy the hollow site in the middle layer. It is found that the diffusion barrier is also less than 0.40 eV when the Li atom occupied the most stable position diffuses along the armchair direction (Fig. 8). The Li ions diffusion energy barriers are lower than those of CEY (0.56 ~ 0.60 eV)[41] and Ti_3C_2 MXene (~0.70 eV).[42]

4. Conclusions

In summary, we elucidated the mechanical properties, lithium adsorption and diffusion character on monolayer and bilayer HsGY using the density functional theory calculations. Firstly, it is found that the monolayer and bilayer HsGY have large critical strains and high in-plane stiffness. Structural deformation will occur during the lithiation cycle, however, lithiated HsGY can well maintain the layered structure. Secondly, the monolayer and bilayer HsGY present strong binding energies upon the adsorption of Li adatoms, and the adsorption interaction between lithium and bilayer HsGY is stronger than the case of monolayer HsGY. Thirdly, the diffusion energy barriers of Li along the surfaces of monolayer and bilayer HsGY are lower than the other 2D materials such as CEY and Ti_3C_2 MXene. Finally, monolayer and bilayer HsGY illustrate ultrahigh charge capacities of 3378 and 2895 mA h g^{-1}, respectively, which distinctly outperform other 2D anode materials. All these results propose that monolayer and bilayer HsGY as outstanding anode materials of LIBs, owing to ultrahigh charge capacity, low diffusive energy barrier, strong interaction and high critical strain.

Conflicts of interest

We declare that we do not have any commercial or associative interest that represents a conflict of interest in connection with the work submitted.

Acknowledgements

This work was financially supported by the National Natural Science Foundation of China under Grant No.11704195, and Qing Lan Project of Jiangsu Province (Grant No. R2019Q04).

References

1 S. Goriparti, E. Miele, F. D. Angelis, E. D. Fabrizio, R. P. Zaccaria and C. Capiglia, Review on recent progress of nanostructured anode materials for Li-ion batteries, *J. Power Sources*, 2014, **257**, 421–443.

2 D. P. Dubal, O. Ayyad, V. Ruiz and P. Gómez-Romero, Hybrid energy storage: the merging of battery and supercapacitor chemistries, *Chem. Soc. Rev.*, 2015, **44**, 1777–1790.
3 C. Ban, Z. Wu, D. T. Gillaspie, L. Chen, Y. Yan, J. L. Blackburn and A. C. Dillon, Nanostructured Fe_3O_4/SWNT electrode: binder-free and high-rate li-ion anode, *Adv. Mater.*, 2010, **22**, E145–E149.
4 G. H. Gelinck, H. E. A. Huitema, *et al.*, Flexible active-matrix displays and shift registers based on solution-processed organic transistors, *Nat. Mater.*, 2004, **3**, 106–110.
5 S. A. Weis, S. E. Sarma, R. L. Rivest and D. W. Engels, Security and privacy aspects of low-cost radio frequency identification systems, *Secur. Pervas. Comput.*, 2004, 2802, pp. 201–212.
6 D. Kim, J. Viventi, J. A. Amsden, J. Xiao, L. Vigeland, *et al.*, Dissolvable films of silk fibroin for ultrathin conformal bio-integrated electronics, *Nat. Mater.*, 2010, **9**, 511–517.
7 S. Y. Chew, S. H. See, J. Wang, P. Novák, F. Krumeich, S. L. Chou, J. Chen and H. K. Liu, Flexible free-standing carbon nanotube films for model lithium-ion batteries, *Carbon*, 2009, **47**, 2976–2983.
8 W. Qi, J. G. Shapter, Q. Wu, T. Yin, G. Gao and D. Cui, Nanostructured anode materials for lithium-ion batteries: principle, recent progress and future perspectives, *J. Mater. Chem. A*, 2017, **5**, 19521–19540.
9 R. Wang, X. Xue, W. Lu, H. Liu, C. Lai, K. Xi, Y. Che, J. Liu, S. Guo and D. Yang, Tuning and understanding the phase interface of TiO_2 nanoparticles for more efficient lithium ion storage, *Nanoscale*, 2015, **7**, 12833–12838.
10 J. Zhu, T. Wierzbicki and W. Li, A review of safety-focused mechanical modeling of commercial lithium-ion batteries, *J. Power Sources*, 2018, **378**, 153–168.
11 J. Liu and X. Liu, Two-dimensional nanoarchitectures for lithium storage, *Adv. Mater.*, 2012, **24**, 4097–4111.
12 Y. Jiao, A. M. Hafez, D. Cao, A. Mukhopadhyay, Y. Ma and H. Zhu, Metallic MoS_2 for high performance energy storage and conversion, *Small*, 2018, **14**, 1800640.
13 Q. Sun, Y. Dai, Y. Ma, T. Jing, W. Wei and B. Huang, *Ab initio* prediction and characterization of Mo_2C monlayer as anodes for lithium-ion for and sodium-ion batteries, *J. Phys. Chem. Lett.*, 2016, **7**, 937–943.
14 T. Yu, Z. Zhao, L. Liu, S. Zhang, H. Xu and G. Yang, TiC_3 monolayer with high specific capacity for sodium-ion batteries, *J. Am. Chem. Soc.*, 2018, **140**, 5962–5968.
15 E. Yoo, J. Kim, E. Hosono, H. Zhou, T. Kudo and I. Honma, Large reversible Li storage of graphene nanosheet families for use in rechargeable lithium ion batteries, *Nano Lett.*, 2008, **8**, 2277–2282.
16 R. H. Baughman, H. Eckhardt and M. Kertesz, Structure–property predictions for new planar forms of carbon: layered phases containing sp^2 and sp atoms, *J. Chem. Phys.*, 1987, **87**, 6687–6699.
17 A. R. Puigdollers, G. Alonso and P. Gamallo, First-principles study of structural, elastic and electronic properties of α-, β- and γ-graphyne, *Carbon*, 2016, **96**, 879–887.
18 Q. Li, Y. Li, Y. Chen, L. Wu, C. Yang and X. Cui, Synthesis of γ-graphyne by mechanochemistry and its electronic structure, *Carbon*, 2018, **136**, 248–254.
19 H. Zhang, M. Zhao, X. He, Z. Wang, X. Zhang and X. Liu, High mobility and high storage capacity of lithium in sp–sp^2 hybridized carbon network: the case of graphyne, *J. Phys. Chem. C*, 2011, **115**, 8845–8850.
20 C. Yang, Y. Li, Y. Chen, Q. Lin, L. Wu and X. Cui, Lithium-ion batteries: mechanochemical synthesis of γ-graphyne with enhanced lithium storage performance, *Small*, 2019, **15**, 1804710.
21 Q. Zhang, C. Tang, W. Zhu and C. Cheng, Strain-enhanced Li storage and diffusion on the graphyne as the anode material in the Li-ion battery, *J. Phys. Chem. C*, 2018, **122**, 22838–22848.
22 M. Makaremi, B. Mortazavi, T. Rabczuk, G. A. Ozin and C. V. Singh, Theoretical investigation: 2D N-graphdiyne nanosheets as promising anode materials for Li/Na rechargeable storage devices, *ACS Appl. Nano Mater.*, 2019, **2**, 127–135.
23 B. Mortazavi, M. Shahrokhi, M. E. Madjet, M. Makaremi and S. T. Rabczuk, N-, P-, As-triphenylene-graphdiyne: strong and stable 2D semiconductors with outstanding capacities as anodes for Li-ion batteries, *Carbon*, 2019, **141**, 291–303.
24 B. Mortazavi, M. Shahrokhi, X. Zhuang and T. Rabczuk, Boron–graphdiyne: a superstretchable semiconductor with low thermal conductivity and ultrahigh capacity for Li, Na and Ca ion storage, *J. Mater. Chem. A*, 2018, **6**, 11022–11036.
25 Z. Yang, C. Zhang, Z. Hou, X. Wang, J. He, X. Li, Y. Song, N. Wang, K. Wang, H. Wang, *et al.*, Porous hydrogen substituted graphyne for high capacity and ultra-stable sodium ion storage, *J. Mater. Chem. A*, 2019, **7**, 11186–11194.
26 X. Ren, X. Li, Z. Yang, X. Wang, J. He, K. Wang, J. Yin, J. Li and C. Huan, Tailoring acetylenic bonds in graphdiyne for advanced lithium storage, *ACS Sustainable Chem. Eng.*, 2020, **8**, 2614–2621.
27 J. Li, S. Li, Q. Liu, C. Yin, L. Tong, C. Chen and J. Zhang, Synthesis of hydrogen-substituted graphyne film for lithium–sulfur battery applications, *Small*, 2019, **15**, 1805344.
28 G. Kresse and J. Furthmüller, Efficient iterative schemes for *ab initio* total-energy calculations using a plane-wave basis set, *Phys. Rev. B: Condens. Matter Mater. Phys.*, 1996, **54**, 11169–11186.
29 G. Kresse and J. Hafner, *Ab initio* molecular dynamics for liquid metals, *Phys. Rev. B: Condens. Matter Mater. Phys.*, 1993, **47**, 558.
30 G. Kresse and D. Schockley, From ultrasoft pseudopotentials to the projector augmented-wave method, *Phys. Rev. B: Condens. Matter Mater. Phys.*, 1999, **59**, 1758–1775.
31 J. P. Perdew, K. Burke and M. Ernzerhof, Generalized gradient approximation made simple, *Phys. Rev. Lett.*, 1996, **77**, 3865–3868.
32 S. Grimme, Semiempirical GGA-type density functional constructed with a long-range dispersion correction, *J. Comput. Chem.*, 2006, **27**, 1787–1799.
33 G. Henkelman, B. P. Uberuaga and H. Jónsson, A climbing image nudged elastic band method for finding saddle points and minimum energy paths, *J. Phys. Chem. C*, 2000, **113**, 9901–9904.

34 Y. Zhang, L. Zhang, H. Pan, H. Wang and Q. Li, Li-decorated porous hydrogen substituted graphyne: a new member of promising hydrogen storage medium, *Appl. Surf. Sci.*, 2021, **535**, 147683.

35 B. Wu, X. Jia, Y. Wang, J. Hu, E. Gao and Z. Liu, Superflexible C_{68}–graphyne as a promising anode material for lithium-ion batteries, *J. Mater. Chem. A*, 2019, **7**, 17357.

36 F. Liu, P. Ming and J. Li, *Ab initio* calculation of ideal strength and phonon instability of graphene under tension, *Phys. Rev. B: Condens. Matter Mater. Phys.*, 2007, **76**, 064120.

37 M. Hankel and D. J. Searles, Li storage on carbon nitride, graphenylene and inorganic graphenylene, *Phys. Chem. Chem. Phys.*, 2016, **18**, 14205–14215.

38 H. J. Hwang, J. Koo, M. Park, N. Park, Y. Kwon and H. Lee, Multilayer graphynes for Li ion battery anode, *J. Phys. Chem. C*, 2013, **117**, 6919–6923.

39 Q. F. Li, C. G. Duan, X. G. Wan and J. L. Ku, Theoretical prediction of anode materials in Li-ion batteries on layered black and blue phosphorus, *J. Phys. Chem. C*, 2015, **119**, 8662–8670.

40 M. K. Aydinol, A. F. Kohan, G. Ceder, K. Cho and J. Joannopoulos, *Phys. Rev. B: Condens. Matter Mater. Phys.*, 1997, **56**, 1354–1365.

41 M. Makaremi, B. Mortazavi and C. V. Singh, Carbon ene-yne graphyne monolayer as an outstanding anode material for Li/Na ion batteries, *Appl. Mater. Today*, 2018, **10**, 115–121.

42 D. Er, J. Li, M. Naguib, Y. Gogotsi and V. B. Shenoy, Ti_3C_2 MXene as a high capacity electrode material for metal (Li, Na, K, Ca) ion batteries, *ACS Appl. Mater. Interfaces*, 2014, **6**, 11173.